iScience

CellPress
OPEN ACCESS

Article

Spontaneous formation of gold nanoparticles on MoS_2 nanosheets and its impact on solution-processed optoelectronic devices

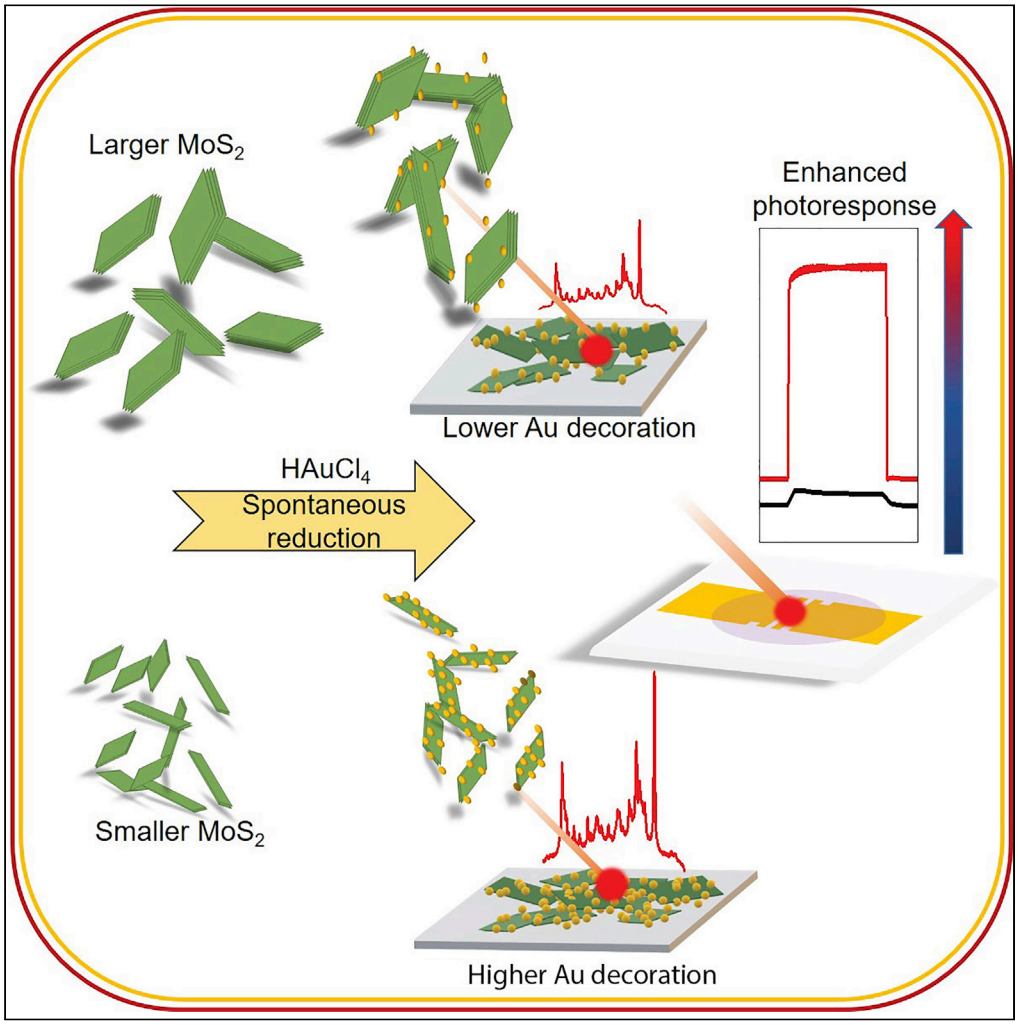

Kenneth Lobo, Vijaya Kumar Gangaiah, Harsha Priya, H. S. S. Ramakrishna Matte

krishnamatte@gmail.com

Highlights

Reducing agent-free Au nanoparticle decoration on aqueously dispersed 2H-MoS_2.

Control on Au nanoparticle decoration density through nanosheet size-selection.

SERS as a probe for determining the decoration density along with microscopy.

Enhanced photodetection by spontaneous modification with Au on MoS_2 films.

Lobo et al., iScience *25*, 104120
April 15, 2022
https://doi.org/10.1016/j.isci.2022.104120

iScience

CellPress
OPEN ACCESS

Article

Spontaneous formation of gold nanoparticles on MoS_2 nanosheets and its impact on solution-processed optoelectronic devices

Kenneth Lobo,[1,2] Vijaya Kumar Gangaiah,[1] Harsha Priya,[1] and H. S. S. Ramakrishna Matte[1,3,*]

SUMMARY

Understanding size-dependent properties of 2D materials is crucial for their optimized performance when incorporated through solution routes. In this work, the chemical nature of MoS_2 as a function of nanosheet size is investigated through the spontaneous reduction of chloroauric acid. Microscopy studies suggest higher gold nanoparticle decoration density in smaller nanosheet sizes, resulting from higher extent of reduction. Further corroboration through surface-enhanced Raman scattering using the gold-decorated MoS_2 nanosheets as substrates exhibited an enhancement factor of 1.55×10^6 for smaller nanosheets which is 7-fold higher as compared to larger nanosheets. These plasmonic-semiconductor hybrids are utilized for photodetection, where decoration is found to impact the photoresponse of smaller nanosheets the most, and is optimized to achieve responsivity of 367.5 mAW^{-1} and response times of ~17 ms. The simplistic modification via solution routes and its impact on optoelectronic properties provides an enabling platform for 2D materials-based applications.

INTRODUCTION

Two-dimensional (2D) materials have been emerging to the forefront for numerous enticing applications. This large family of materials is found to be versatile and diverse in properties, encompassing interesting materials such as topological insulators, semiconductors, and superconductors (Choudhary et al., 2017; Lu et al., 2019; Sun et al., 2011; Teweldebrhan et al., 2010). Semiconducting 2D materials like transition metal dichalcogenides have shown promise for several applications in memory and computing circuits, and for optoelectronic devices such as photodetectors, light-emitting devices, and solar cells (Dathbun et al., 2017; Huh et al., 2020; Jariwala et al., 2014; Tsai et al., 2014; Wang et al., 2012a, 2012b). The vast scope for their applicability and possible commercialization mandates the need to produce high-quality 2D materials in large quantities. Among synthetic protocols, solution routes offer significant advantages through scalability, ambient processability, speedy, and additive manufacturability, and are less demanding compared to traditional techniques (Bonaccorso et al., 2016; Hassan et al., 2020; Nicolosi et al., 2013; Varrla et al., 2015). In this regard, the protocol of liquid-phase exfoliation has enabled the processing of numerous 2D materials (Bellani et al., 2021; Bonaccorso et al., 2016; Cao et al., 2016; Coleman et al., 2011; Ma and Sasaki, 2015). Detailed investigations have probed the underlying aspects of solvent suitability, and suggest a predominant role of Hansen solubility parameters and surface tension components to enable stable and concentrated nanosheet dispersions (Coleman et al., 2011; O'Neill et al., 2012; Wang et al., 2017; Zhou et al., 2011). These insights have enabled the production of dispersions in suitable organic solvents and mixed-solvent systems. Aqueous dispersions have also been produced, most often through the use of additives such as surfactants in order to obtain stability (Guardia et al., 2014; Lotya et al., 2009; Maleski et al., 2017; McManus et al., 2017).

An inherent attribute of liquid-exfoliated nanosheets is the large polydispersity in size, both in lateral dimensions and in number of layers. The physiochemical properties of 2D materials have been found to be highly size dependent, thus making it vital to address the polydispersity in liquid-exfoliated nanosheets. For example, addition of larger nanosheets as fillers has been shown to exhibit enhanced mechanical properties in polymer nanocomposites when compared to smaller nanosheets (O'Neill et al., 2012). Similarly, the electrocatalytic activity in hydrogen evolution reaction is found to increase with decreasing flake size (Harvey et al., 2015; Seo et al., 2015; Varrla et al., 2015; Wang et al., 2013). In photodetectors, the

[1]Centre for Nano and Soft Matter Sciences, Arkavathi Campus, Survey No.7, Shivanapura, Dasanapura Hobli, Bengaluru 562162, India

[2]Manipal Academy of Higher Education, Manipal 576 104, India

[3]Lead contact

*Correspondence: krishnamatte@gmail.com

https://doi.org/10.1016/j.isci.2022.104120

density of trap states in networks of interconnected nanosheets has been found to be dependent on nanosheet size, in turn having an impact on the device response time (Alzakia et al., 2020b). Thus, gaining an understanding into size-dependent properties is crucial for the optimal applicability of 2D materials through solution routes. To narrow down polydispersity, various centrifugation-based separation protocols have been devised, with liquid cascade centrifugation being simple and high-throughput in nature (Backes et al., 2014, 2019; Kang et al., 2014; Ogilvie et al., 2019).

Aqueous dispersions offer several obvious advantages in processing, although the use of stabilizing additives could have detrimental effects on properties such as conductivity (Secor et al., 2013, 2015). In this regard, aqueous additive-free dispersions hold vast potential for a diverse variety of applications, especially those involving biological systems (Kaur et al., 2018; Lobo et al., 2021). In addition to this, aqueous dispersions enable suitable modification of nanosheets for application-tailored properties (Ma et al., 2020). Similarly, modification of 2D materials using other nanomaterials has also been evaluated and is found to synergistically augment their capabilities. Of special interest are 2D material systems with noble metal nanoparticles to form hybrids. Such modification could have interesting implications through the introduction of phenomena, such as enhanced light absorption through plasmonics (Tu and Wu, 2021; Yin et al., 2014), and better electron transport through efficient charge transfer and increased conductivity (Goswami et al., 2019). To synthesize such systems, several approaches have been made. Physical deposition approaches such as sputtering have been used, although this method is limited to coating prefabricated films of 2D materials on substrates (DiStefano et al., 2020; Li et al., 2020b; Rahmati et al., 2019). Direct addition of nanoparticles is another adopted route, although the process for first growing such nanoparticles forms a separate synthesis step and involves the use of reducing agents (Pramanik et al., 2019). In this regard, transition metal dichalcogenides possess a rich chemistry, which enables them to reduce metal precursors such as $HAuCl_4$, resulting in Au nanoparticle decoration through solution-processable protocols (Grieger et al., 2020; Kim et al., 2013; Polyakov et al., 2014). The spontaneity of this reduction reaction arises from the intrinsic chemical nature of the nanosheets and effectively bypasses the need for additional synthetic processes and associated use of chemicals. For example, the extent of $HAuCl_4$ reduction has been shown to be influenced by the phase of $MoTe_2$ nanosheets obtained from chemical vapor deposition with the 1T′ phase being more energetically favorable, while the dechlorination on 2H-$MoTe_2$ occurs favorably only on defect sites (Tao et al., 2021). Other 2D materials such as GaTe obtained from micromechanical cleavage have also demonstrated spontaneous reducing ability leading to Au nanoparticle decoration and has been attributed to monoclinic structure and defects (Lu et al., 2018). Given the tremendous influence Au nanoparticle decoration could have on properties of semiconducting transition metal dichalcogenide nanosheets, this simplistic synthetic protocol could have a lot to offer. The extent of such implications on the properties of 2D materials leverages the need to understand the factors of control, in order to develop suitable methods to obtain such hybrids. Although a variation in chemical properties based on nanosheet size is known to occur, its influence on such spontaneous reduction reactions remains unexplored and draws interest, given the scope for tunability in properties through optimal modification with noble metal nanoparticles.

In this work, we explore the ability to suitably modify MoS_2 nanosheets by carrying out spontaneous reactions in an aqueous surfactant-free media. The role of nanosheet size on the chemical activity is probed through the reduction of $HAuCl_4$ to Au nanoparticles by MoS_2. Size-selected nanosheets were systematically reacted with different amounts of Au precursor without the need for additional reducing agents, and the extent of Au nanoparticle decoration was investigated using transmission electron microscopy. A higher coverage of the nanosheets with the Au nanoparticles was observed in smaller MoS_2 nanosheets, and could be resulting from their relatively higher defect density. To support these observations, the decorated MoS_2 nanosheets have been used as substrates in surface-enhanced Raman scattering and the enhancement factors were found to increase with decreased nanosheet size reaching 1.55×10^6. In addition to this, the role of nanoparticle decoration on light-matter interactions in this plasmonic-semiconductor Au-MoS_2 system is evaluated in the domain of optoelectronics using solution-processed photodetectors. Significant enhancements in photoresponse were observed with increasing Au decoration, especially in the case of smaller nanosheets. Optimal Au loading was achieved simply by dipping MoS_2-coated devices in $HAuCl_4$, and the fabricated devices exhibited responsivity up to 367.5 mAW^{-1}, with a rise and decay time of ~17 ms. This simplistic protocol powered by the intrinsic size-dependent chemical nature of liquid-exfoliated nanosheets provides a design factor for precise tailoring of light-matter interactions in 2D materials.

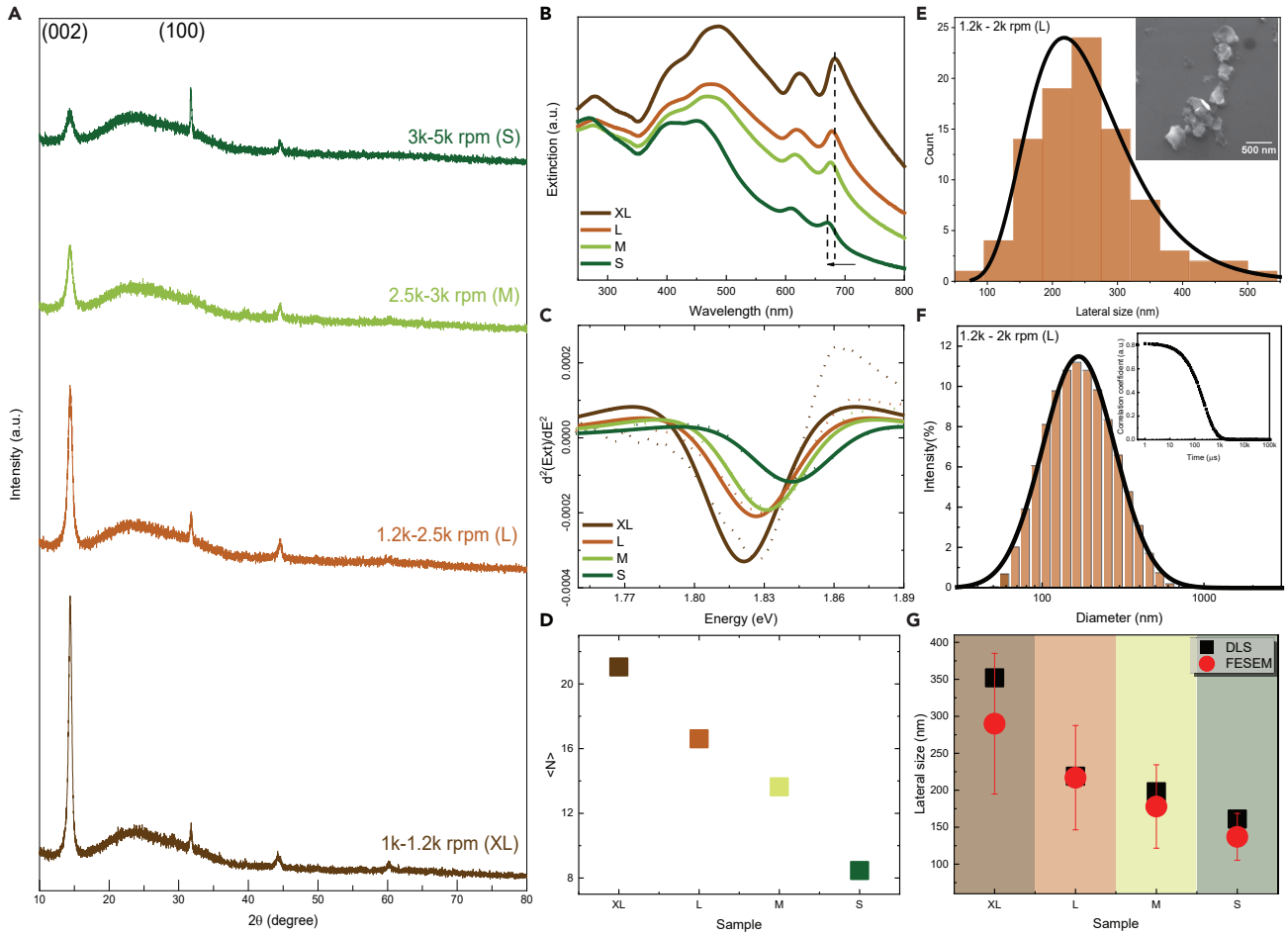

Figure 1. Characterization of size-selected aqueous MoS_2 nanosheet dispersions

(A) X-ray diffractograms of MoS_2 nanosheets size-selected at various centrifugation speeds.

(B and C) (B) UV-visible extinction spectra of the size-selected dispersions and (C) the double derivative of the A-exciton peak with Lorentzian peak fitting.

(D) Calculated number of layers, as obtained by the position of the A-exciton peak.

(E and F) (E) Statistical histogram of the lateral dimensions of nanosheets obtained between 1.2 and 2 krpm through FESEM image analysis (as pictured in the inset, scale bar: 500 nm)) and (F) mean hydrodynamic diameter through dynamic light scattering (inset: correlogram).

(G) Comparison of nanosheet lengths as obtained through FESEM statistics and light scattering.

RESULTS AND DISCUSSIONS

To investigate the implications of nanosheet dimensions on their chemical reactivity in the spontaneous reduction of $HAuCl_4$, obtaining nanosheets of well-defined size is crucial. Here, size selection was carried out by a cascaded centrifugation protocol. The resulting sediments fractionated at successively higher centrifugation speeds from such protocols are shown to systematically decrease in lateral dimensions and thickness (Backes et al., 2016a, 2016b, 2016c, 2017).

To determine the dimensions of the size-selected nanosheets, various methods were employed. Figure 1A shows the x-ray diffractogram of nanosheets obtained at successively progressing sedimentation speeds from 1.2 krpm to 5 krpm. The intensity of the (002) reflection of MoS_2 appearing at ~14.4° is found to reduce relative to other characteristic material peaks and increase in full-width at half maximum (Figure S1), which further indicates a reduction in nanosheet thickness separated at higher centrifugation speeds. The extinction spectra of MoS_2 as shown in Figure 1B contain characteristic peaks from exciton transitions arising from splitting of the valence band at the high symmetry point. This, along with the Raman spectra (Figure S2) indicates retention in the chemical nature of MoS_2 after exfoliation and re-dispersion in water. Through extensive experimental corroborations between UV-visible spectroscopy and atomic force microscopy, the

position of the A-exciton transition (observed at ~ 670 nm) has been correlated to the number of layers through an empirical formula (Backes et al., 2014). To determine the number of layers, the double-derivative of the A-exciton peak with respect to incident wavelength was fitted with Lorentzian profiles, as shown in Figure 1C. The number of layers obtained by this metric suggested the separation of thick nanosheets between 1 and 1.2 krpm to comprise ~21 layers, subsequently reducing to ~17 layers between 1.2 and 2.5 krpm, ~14 layers between 2.5 and 3 krpm, and ~8 layers between 3 krpm and 5 krpm, as represented in Figure 1D. A general trend observed in liquid exfoliation is the production of thicker nanosheets with larger lateral dimensions, which reduce in size as they get thinner. To determine the lateral dimensions of the nanosheets, field emission scanning electron microscopy (FESEM) image analysis, as well as dynamic light scattering (DLS) were carried out. FESEM images of the size-selected nanosheets were analyzed using ImageJ software to obtain distribution histograms. For the sample obtained between 1.2 and 2 krpm, the obtained distribution is as shown in Figure 1E, along with a lognormal fitting. The hydrodynamic diameter inferred from DLS for this sample is as shown in Figure 1F. Respective plots for the other sizes are represented in the supporting information (Figure S3). The lateral sizes as determined by FESEM statistics were found to be 290 $\pm$ 95 nm (1–1.2 krpm), 217 $\pm$ 70 nm (1.2–2.5 krpm), 178 $\pm$ 56 nm (2.5–3 krpm), and 137 $\pm$ 31 nm (3–5 krpm). Similarly, by DLS, the hydrodynamic diameters were determined to be 352 nm (1–1.2 krpm), 219 nm (1.2–2.5 krpm), 198 nm (2.5–3 krpm), and 161 nm (3–5 krpm). Shown in Figure 1G are the lateral dimensions of the four samples, showing good agreement between both techniques. Thus by using centrifugation based separation protocols in a cascaded sequence, well size-separated dispersions can be obtained with reduced polydispersity. For ease, the samples are hereby referred to as extra-large (XL-MoS_2, 1–1.2 krpm), large (L-MoS_2, 1.2–2.5 krpm), medium (M−MoS_2, 2.5–3 krpm), and small (S-MoS_2, 3–5 krpm) accordingly. In addition to probing size, the zeta potentials of the nanosheets were obtained in aqueous media (Figure S4). The nanosheets in all samples were found to bear a negative charge which could be arising from the dangling bonds along the edges, resulting in dispersion stability (Coleman, 2009).

Upon obtaining dispersions with controlled and well-characterized nanosheet size, we carried out Au nanoparticle decoration through a spontaneous reduction of $HAuCl_4$ using MoS_2. This reaction is enabled through a suitable alignment of the energy levels between MoS_2 and $AuCl_4^-$, which results in a spontaneous electron transfer (Grieger et al., 2020; Kim et al., 2013; Polyakov et al., 2014; Song et al., 2018; Yuan et al., 2019). As also observed for other 2D materials, the reduction occurs preferably at defect sites owing to favorable energetics (Lu et al., 2015, 2018; Tao et al., 2021), and results in the growth of Au nanoparticles. Here, we show extensive characterization for the size-selected MoS_2 nanosheets. The UV-visible extinction spectra of MoS_2 dispersions when mixed with increasing amounts of $HAuCl_4$ are as shown in Figure S5, showing a heightening intensity of the Au plasmonic peak around 550 nm, which is red-shifted with increasing Au concentration. By tuning the reaction concentrations, the plasmonic activity of Au nanoparticles prepared using this method can be suitably tuned (Lin et al., 2020). In order to probe the effect of nanosheet dimensions on $HAuCl_4$ reduction, the size-selected MoS_2 nanosheets were reacted with 2 and 4 equivalents of $HAuCl_4$, taken in equal volumes of 1 mL. The x-ray diffractogram of the decorated MoS_2 nanosheets (obtained by reacting with 4 equivalents of $HAuCl_4$) are as shown in Figure S6, suggesting crystallinity of the nanoparticles. In the case of XL-MoS_2 and L-MoS_2, the (002) peak from MoS_2 presents itself along with reflections from the Au lattice. These observations of reducing agent-free crystalline nanoparticle growth on MoS_2 nanosheets occur at room temperature and without the use of demanding synthetic conditions, thus strengthening the capabilities of aqueous dispersions in performing modifications.

Transmission electron microscopy (TEM) was used to evaluate the decoration density and crystallinity of the Au nanoparticles grown on the nanosheets. The nucleation and growth of the Au nanoparticles is dependent on the chemical activity of the nanosheets and by the amount of Au precursor available for reaction. In order to probe the effect of nanosheet size on these aspects, we have analyzed micrographs obtained using TEM. Shown in Figures 2A and 2B are representative TEM images of the XL-MoS_2 nanosheets reacted with 2 and 4 equivalents of $HAuCl_4$, respectively. Similarly, shown in Figures 2C and 2D are representative images of S-MoS_2 nanosheets decorated under similar concentrations. An increased decoration density was observed at 4 equivalents as compared to 2 equivalents, which could be due to the higher availability of Au precursor for the reaction. Similar observations can be made for both XL-MoS_2 and S-MoS_2 with respect to the reaction concentrations. On comparing the decoration based on nanosheet size, a much higher decoration density is found to have occurred in S-MoS_2 as compared to XL-MoS_2 for both 2 and 4 equivalents of $HAuCl_4$. As $HAuCl_4$ reduction is observed to occur preferentially along edges and defects (Kim et al., 2013; Polyakov et al., 2014), its higher density in smaller nanosheets could be the driving factor

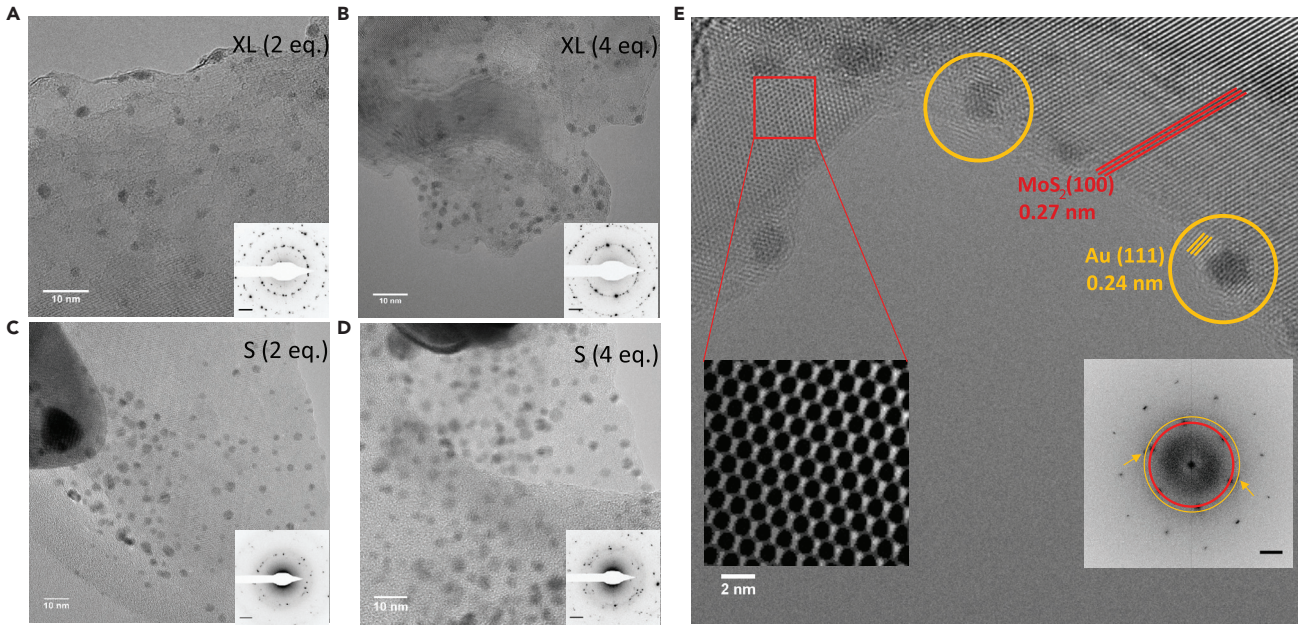

Figure 2. Transmission electron microscopy of Au-decorated MoS_2 nanosheets

(A–D) Low magnification TEM image of XL-MoS_2 nanosheets reacted with (A) 2 equivalents and (B) 4 equivalents, and S-MoS_2 nanosheets reacted with (C) 2 equivalents and (D) 4 equivalents of $HAuCl_4$ (Scale bar: 10 nm) respectively along with their electron diffraction patterns (scale bar: 2 nm^{-1}).

(E) High-resolution TEM image of Au nanoparticle (yellow circles)-decorated MoS_2 nanosheet (Scale bar: 2 nm), with insets of a magnified processed region and fast Fourier transform (scale bar: 2 nm^{-1}).

for the reaction and subsequent Au nanoparticle decoration. In addition to the decoration density of Au nanoparticles populating the nanosheets, a further evaluation of the effect of nanosheet dimensions on nanoparticle size was performed by comparing the statistical histograms of ~350 nanoparticles (Figure S7). The Au nanoparticles grown on XL-MoS_2 were found to have a slight increase as reaction concentrations increased from 2 to 4 equivalents, with mean diameters of 2.35 and 2.67 nm, respectively. As for the case of S-MoS_2, slightly larger Au nanoparticles with a mean diameter of 3.35 nm for 2 equivalents and 3.69 nm for 4 equivalents were found, respectively. In the case of S-MoS_2, some large as well as free Au particles were also observed (Figure S8). Thus, Au nanoparticle decoration on MoS_2 nanosheets through the spontaneous reduction of $HAuCl_4$ is found to be dependent not only on the precursor concentration but also on the MoS_2 nanosheet dimensions, suggesting their size-dependent reducing ability.

Figure 2E shows a representative high-resolution TEM image of Au-decorated MoS_2. The crystallinity of Au nanoparticles (circled in yellow) can be inferred from the periodic spacing which was found to be 0.24 nm, and can be indexed to the (111) plane. The periodicity in the supporting MoS_2 nanosheet can also be seen (as shown in red) with a spacing of 0.27 nm, which can be indexed to the (100) plane. This periodicity for both MoS_2 and Au is also observed in the Fourier transformed image (inset) as well. A processed magnified inset of the region marked by a square shows the hexagonal lattice formed by the Mo and S atoms. The lattice spacing observed through high-resolution TEM images is in agreement with the selected area electron diffraction (SAED) and x-ray diffraction patterns, thereby confirming the crystalline nature of both MoS_2 and the Au nanoparticles. Similar observations on nanosheet and nanoparticle crystallinity were observed for both investigated nanosheet sizes.

In order to further investigate the extent of Au decoration on the size-selected nanosheets and their impact on light-matter interactions, we explored the use of the decorated nanosheets as substrates for surface-enhanced Raman scattering. Plasmonic nanoparticles have been shown to enhance the intensity of Raman signals, even down to single molecule level by enhancing the local electromagnetic field, while non-plasmonic semiconducting platforms can also result in enhancements through transitions occurring via charge transfer (Camden et al., 2008; Lee et al., 2016; Lombardi and Birke, 2012, 2014; Sun et al., 2014). A dependence of phase of the transition metal dichalcogenide has also been shown to dictate the extent of decoration, and also affect the contributions of chemical enhancement (Tao et al., 2021). To investigate the

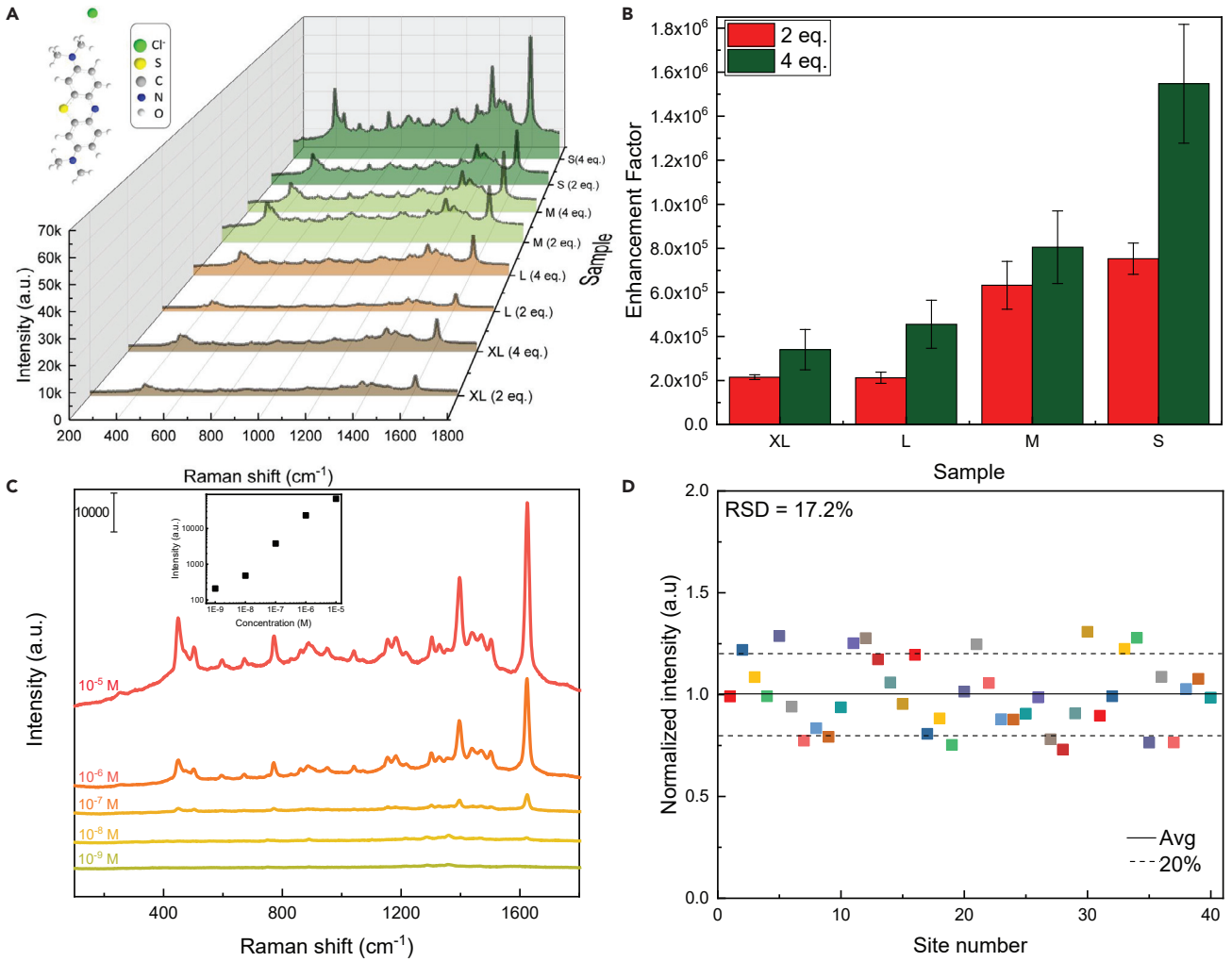

Figure 3. Au-decorated MoS_2 nanosheets as SERS substrates

(A and B) (A) SERS spectra of methylene blue molecule (inset) on substrates of size-selected MoS_2 nanosheets reacted with different amounts of $HAuCl_4$, and the (B) calculated enhancement factors of the respective SERS substrates.

(C) Spectra for different concentrations of the dye on the S-MoS_2 (4 eq.) substrates and the calibration plot in the inset.

(D) Normalized intensity plot with the relative standard deviation of the Au-MoS_2 substrates in detection of methylene blue.

contrasting decoration densities observed by TEM, the decorated size-selected nanosheets were used as substrates for SERS with methylene blue dye as a reporter molecule.

The SERS activity of the substrates was evaluated by determining the enhancement factors (EF), and a comparison was made between the size-selected nanosheets decorated to different densities. The EF for an SERS substrate is calculated using the formula,

$$EF = (I_{SERS}/I_{Raman}) \times (N_{Raman}/N_{SERS})$$

where, I_{SERS} and I_{Raman} represent the intensity of the SERS signal from the reporter molecule on the Au-MoS_2 substrate (taken at a concentration of 10 μM), and the intensity of the reporter molecule powder, respectively. N_{Raman} and N_{SERS} represent the number of molecules in the powder, and on the SERS substrate under illumination, respectively. Here, the Raman peak at 1624 cm^{-1} was considered for calculations, which arise from the stretching of the C-C bonds in the aromatic ring (Nicolai and Rubim, 2003; Xiao and Man, 2007). Further details regarding the calculation of the EF are provided in the supporting information. The spectra of methylene blue on various sample substrates are presented in Figure 3A. It was observed

that with denser Au nanoparticle decoration, the intensity of the Raman signals was found to be increased. In addition to this, smaller nanosheets reacted under similar conditions to that of larger nanosheets were found to have higher intensities. The enhancement factors were calculated, and are as represented in Figure 3B. For XL-MoS_2 (2 eq.), the enhancement factor was calculated to be 2.15×10^5 ($\pm 1 \times 10^4$), while for S-MoS_2 (4eq.) the value was found to be approximately 7 times higher at 1.55×10^6 ($\pm 26.9 \times 10^4$). S-MoS_2 reacted with 2 equivalents had an enhancement factor which is ~2.2 times higher than that of XL-MoS_2 reacted with 4 equivalents. Such enhancement in EF is a result of optimized Au precursor concentration and the size of MoS_2 nanosheets. The EF calculated here through size-selection of MoS_2 nanosheets is in par with previously reported protocols, although to note that it is achieved via an all solution route without the need for demanding synthetic conditions or chemicals (Chen et al., 2020; Lv et al., 2020; Su et al., 2014; Tegegne et al., 2020).

The peak intensity for lower concentrations of methylene blue was investigated on the S-MoS_2 (4 equivalents) substrates as shown in Figure 3C, and were found to detect concentrations as low as 1 nM. The dependence of peak intensity on analyte concentration is as shown in the inset of Figure 3C. In order to find the variation in intensity across various positions on the substrate, multiple areas were probed (40 points). The normalized peak intensity at 1624 cm^{-1} for all points is as represented in Figure 3D, demonstrating a relative standard deviation (RSD) of only about 17.2%. In addition, the stability of the Au-MoS_2 substrates was also investigated. By comparing freshly prepared substrates to 5-month-old substrates stored in ambient conditions, the signal intensities were found to be highly reproducible and showcase the stability of the decorated nanosheets (Figure S9). These observations suggest the plausible usage of these substrates in analyte detection.

To evaluate the influence of plasmonic noble metal nanoparticles on the semiconducting MoS_2 platform, their applicability in photodetection was studied. The Au decoration was carried out as depicted in the schematic in Figure 4A. MoS_2 dispersions were spray coated onto Au gap electrodes on glass substrates, which were then dipped into $HAuCl_4$ solution for different intervals of time in order to carry out nanoparticle decoration. The interest is to obtain high-performance photodetectors with as low Au metal loading. Optimization of the dipping time is essential to prevent a direct pathway for conduction through interconnected Au nanoparticles that could result in electrical shorting, while also ensuring as minimal Au metal content as possible. Presented in Figure S11 are the photoresponses of devices comparing bare MoS_2 to those decorated for 1 and 2 min, for both XL-MoS_2 and S-MoS_2. Higher dark currents were observed in XL-MoS_2 nanosheet films as compared to S-MoS_2 nanosheet films and could possibly be due to the lesser number of inter-nanosheet junctions in larger nanosheets films (Kelly et al., 2021). Upon illumination, higher photocurrents were observed in bare XL-MoS_2 (18.5 pA) as compared to bare S-MoS_2 (3.8 pA). After 1 min of dipping the XL-MoS_2 and S-MoS_2 devices, the photocurrent was found to be significantly enhanced to 600 and 352 pA, respectively. However, after 2 min of dipping, XL-MoS_2 shows a marginal rise to 619 pA, whereas S-MoS_2 further increased to 676 pA. The improvement in photocurrents seen in S-MoS_2 as compared to XL-MoS_2 could be a result of the higher reducing ability which leads to denser Au nanoparticle decoration. Therefore, further optimizations with respect to dipping time were carried out with S-MoS_2 alone. It was found that a dipping time of 5 min produced a significant improvement in photocurrents, beyond which the performance reduced and could be coming from electron-hole recombination in the films. The I-V characteristics for S-MoS_2 decorated by dipping for 5 min are as shown in Figure 4B. Significantly higher currents were observed under illuminated conditions. Compared to the bare MoS_2 device (inset), the dark currents were also considerably higher, suggesting decreased resistance from the Au nanoparticle decoration. Photocurrent responses obtained under increasing bias potentials are shown in Figure 4C. The photocurrent response as a function of incident optical power was evaluated at a bias potential of 15 V and the figures of merit for photodetectors calculated. The photocurrent exhibited a dependence on optical power with a factor of 0.31. The responsivity and photocurrents at different incident optical power are as represented in Figure 4D. The responsivity was found to vary exponentially with the incident power by a factor of −0.68. At an optical input of 1.46 μW mm^{-2}, the device exhibited a responsivity of 367.5 mA W^{-1}, and a specific detectivity of $2.95*10^8$ Jones. The response time of the photodetectors was also probed (Figure S12). The rise time was found to be 17.8 ms and the decay time was found to be 16.8 ms. A comparison of the figures of merit for our photodetectors and literature reported photodetectors are provided in the supporting information (Table S1). The devices demonstrated here perform superior to reported MoS_2 based photodetectors with Au nanoparticles in terms of responsivity and response time (Guo et al., 2019; Lin et al., 2020; McManus et al., 2018; Rahmati et al., 2019; Selamneni et al., 2021).

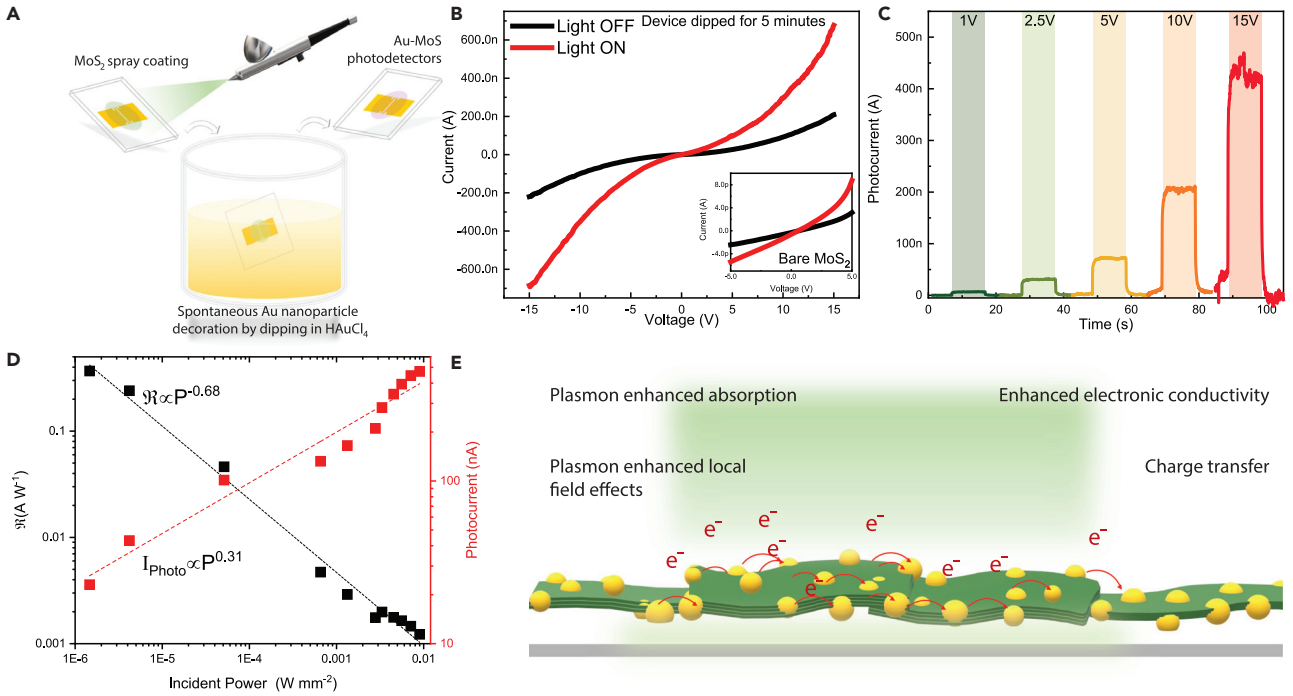

Figure 4. Device characterization of Au-decorated MoS_2 nanosheets

(A) Protocol for fabrication of solution-processed photodetectors by spray coating MoS_2 and Au nanoparticle decoration by dipping in $HAuCl_4$.

(B) Current versus voltage characteristics of a device prepared after a 5 min dip in $HAuCl_4$.

(C) Variation in photocurrents with bias potential.

(D) Responsivity and specific detectivity as a function of incident optical power on the device biased at 15 V.

(E) Schematic representing the possible influence of the Au nanoparticles on the MoS_2 nanosheets in photodetection.

Comparisons with reports on solution-processed transition metal dichalcogenide-based photodetectors have also been made (Abid et al., 2019; Alzakia et al., 2020a, 2020b; Kim et al., 2021; Li et al., 2020a; Liu et al., 2019; McManus et al., 2017; Pulikodan et al., 2020; Seo et al., 2019).

A few of the plausible mechanisms through which enhancement in device performance is observed through Au nanoparticle decoration are as outlined in Figure 4E. The plasmonic resonance from the Au nanoparticles could be increasing the optical absorbance as compared to bare MoS_2, as suggested by the UV-visible absorbance spectra (Figure S5). Additionally, the fields generated between plasmonic nanoparticles that produce an electromagnetic enhancement in SERS could be operating in an analogous fashion by greatly amplifying the localized electric fields in the semiconducting MoS_2 nanosheets, thereby enhancing the photogeneration of electrons upon irradiation (Lin et al., 2013; Miao et al., 2015). Besides these plasmonic-induced effects, the Au nanoparticles that are rooted to the underlying nanosheet substrates form a good interface for charge transfer from the optically active MoS_2 nanosheets (Singha et al., 2018; Sreeprasad et al., 2013). This is supported by observations of shifted (and enhanced) Raman peaks after decoration as shown in Figures S5 and S10. This was found to be more prominent in the case of S-MoS_2 as compared to XL-MoS_2. The presence of the metal nanoparticles also substantially increases the electrical conductivity of the film, when compared to bare MoS_2 nanosheets as observed from the I-V characteristics. The photoresponse of MoS_2 photodetectors was thus improved by a great margin through Au nanoparticle decoration through a facile process of dipping the device in $HAuCl_4$ solution. The synthetic protocol reported here for Au nanoparticle decoration was also found to be applicable to other aqueously dispersed transition metal dichalcogenides such as $MoSe_2$, WS_2, and WSe_2, suggesting the broad scope for modifying 2D materials (Figures S13 and S14). Crystalline nanoparticles were found to grow spontaneously on the nanosheet surfaces as inferred from x-ray diffractograms as shown in Figure S13A. The absorption characteristics are similar to that of MoS_2 and the presence of the plasmonic nature is attributed to the formation of the Au nanoparticles (Figures S13B and S13D). The Raman spectra of the decorated nanosheets also suggested a retention in their chemical nature (Figures S13E–S13G). Transmission electron microscopy further confirms the decoration of the nanosheets with crystalline Au nanoparticles (Figure S14).

Conclusions

The investigations presented here focus on the scope for modification of MoS_2 nanosheets for optoelectronic applications. By utilizing size-selected nanosheets for the spontaneous chemical reduction of chloroauric acid, Au nanoparticle decoration on the nanosheets was obtained in aqueous medium under ambient conditions without the use of reducing agents. Crystalline nanoparticle growth with varying decoration densities was observed through investigations by electron microscopy and SERS, suggesting a size dependent chemical nature of MoS_2 nanosheets. Smaller decorated nanosheets were found to exhibit 7-fold higher enhancement factors as compared to the larger nanosheets, reaching as high as 1.55×10^6. The implications of Au nanoparticle decoration on MoS_2 nanosheets in photodetection were evaluated through solution routes, by dipping spray coated MoS_2 devices into a solution of $HAuCl_4$. Similar to the observations from SERS, smaller nanosheets were found to be affected profoundly. Optimized Au metal loading yielded devices with a fast response time of ~17 ms, while achieving a responsivity of 367.5 mAW^{-1}. These findings suggest the scope for suitable modifications of various 2D materials through spontaneous metal nanoparticle formation together with size-control could enhance their performance in various applications using solution-processed techniques.

Limitations of the study

The protocol for Au decoration outlined in our work relies on the higher defect density in smaller nanosheets, although in order to gain a further understanding into the underlying phenomenon, the kinetics of nucleation and growth need detailed investigation. Theoretical studies may in this case provide a deeper understanding in to the observed higher activity of smaller nanosheets as compared to larger nanosheets. In order to investigate the implications of decoration density, SERS has been used as a tool here, although the underlying factors warrant a detailed investigation in order to discern electromagnetic and charge-transfer contributions. Enhanced photoresponse of nanosheets with Au nanoparticle decoration has been evaluated in this work; however, there is a scope for further optimization for better figures of merit in solution-processed photodetectors, to be in par with photodetectors obtained using other synthetic strategies such as chemical vapor deposition and mechanical cleavage.

STAR★METHODS

Detailed methods are provided in the online version of this paper and include the following:

- KEY RESOURCES TABLE
- RESOURCE AVAILABILITY
  - Materials availability
  - Date and code availability
- METHOD DETAILS
  - Exfoliation and size-selection
  - Au nanoparticle decoration
  - Characterization techniques
  - Surface enhanced raman scattering
  - Solution-processed photodetectors

SUPPLEMENTAL INFORMATION

Supplemental information can be found online at https://doi.org/10.1016/j.isci.2022.104120.

ACKNOWLEDGMENTS

The authors acknowledge the Central Research Facility, Centre for Nano and Soft Matter Sciences, Bengaluru for facilities. HSSRM acknowledges funding from Core Research Grant, SERB, DST (Grant No. CRG/2019/002963). KL thanks CeNS for fellowship.

AUTHOR CONTRIBUTIONS

KL planned the work, prepared aqueous dispersions along with HP, carried out Raman and photodetection measurements, and wrote the paper. VKG carried out the Au decoration and helped with Raman spectroscopy. HSSRM conceived the project and supervised the work. All authors discussed and helped prepare the manuscript.

DECLARATION OF INTERESTS

The authors have no conflicts to declare.

Received: December 3, 2021
Revised: February 28, 2022
Accepted: March 16, 2022
Published: April 15, 2022

REFERENCES

Abid, Sehrawat, P., and Islam, S. (2019). Broadband photodetection in wide temperature range: layer-by-layer exfoliation monitoring of WS_2 bulk using microscopy and spectroscopy. J. Appl. Phys. *125*, 154303. https://doi.org/10.1063/1.5080922.

Alzakia, F.I., Jonhson, W., Ding, J., and Tan, S.C. (2020a). Ultrafast exfoliation of 2D materials by solvent activation and one-step fabrication of all-2D-material photodetectors by electrohydrodynamic printing. ACS Appl. Mater. Interf. *12*, 28840–28851. https://doi.org/10.1021/acsami.0c06279.

Alzakia, F.I., Tang, B., Pennycook, S.J., and Tan, S.C. (2020b). Engineering the photoresponse of liquid-exfoliated 2D materials by size selection and controlled mixing for an ultrasensitive and ultraresponsive photodetector. Mater. Horiz. *7*, 3325–3338. https://doi.org/10.1039/D0MH01493A.

Backes, C., Campi, D., Szydlowska, B.M., Synnatschke, K., Ojala, E., Rashvand, F., Harvey, A., Griffin, A., Sofer, Z., and Marzari, N. (2019). Equipartition of energy defines the size–thickness relationship in liquid-exfoliated nanosheets. ACS Nano *13*, 7050–7061. https://doi.org/10.1021/acsnano.9b02234.

Backes, C., Hanlon, D., Szydlowska, B.M., Harvey, A., Smith, R.J., Higgins, T.M., and Coleman, J.N. (2016a). Preparation of liquid-exfoliated transition metal dichalcogenide nanosheets with controlled size and thickness: a state of the art protocol. J. Vis. Exp. *118*, e54806.

Backes, C., Higgins, T.M., Kelly, A., Boland, C., Harvey, A., Hanlon, D., and Coleman, J.N. (2017). Guidelines for exfoliation, characterization and processing of layered materials produced by liquid exfoliation. Chem. Mater. *29*, 243–255. https://doi.org/10.1021/acs.chemmater.6b03335.

Backes, C., Paton, K.R., Hanlon, D., Yuan, S., Katsnelson, M.I., Houston, J., Smith, R.J., McCloskey, D., Donegan, J.F., and Coleman, J.N. (2016b). Spectroscopic metrics allow in situ measurement of mean size and thickness of liquid-exfoliated few-layer graphene nanosheets. Nanoscale *8*, 4311–4323. https://doi.org/10.1039/C5NR08047A.

Backes, C., Smith, R.J., McEvoy, N., Berner, N.C., McCloskey, D., Nerl, H.C., O'Neill, A., King, P.J., Higgins, T., and Hanlon, D. (2014). Edge and confinement effects allow in situ measurement of size and thickness of liquid-exfoliated nanosheets. Nat. Commun. *5*, 1–10. https://doi.org/10.1038/ncomms5576.

Backes, C., Szydłowska, B.M., Harvey, A., Yuan, S., Vega-Mayoral, V., Davies, B.R., Zhao, P.-l., Hanlon, D., Santos, E.J., and Katsnelson, M.I. (2016c). Production of highly monolayer enriched dispersions of liquid-exfoliated nanosheets by liquid cascade centrifugation. ACS Nano *10*, 1589–1601. https://doi.org/10.1021/acsnano.5b07228.

Bellani, S., Bartolotta, A., Agresti, A., Calogero, G., Grancini, G., Di Carlo, A., Kymakis, E., and Bonaccorso, F. (2021). Solution-processed two-dimensional materials for next-generation photovoltaics. Chem. Soc. Rev. *50*, 11870–11965. https://doi.org/10.1039/D1CS00106J.

Bonaccorso, F., Bartolotta, A., Coleman, J.N., and Backes, C. (2016). 2D-crystal-based functional inks. Adv. Mater. *28*, 6136–6166. https://doi.org/10.1002/adma.201506410.

Camden, J.P., Dieringer, J.A., Wang, Y., Masiello, D.J., Marks, L.D., Schatz, G.C., and Van Duyne, R.P. (2008). Probing the structure of single-molecule surface-enhanced Raman scattering hot spots. J. Am. Chem. Soc. *130*, 12616–12617. https://doi.org/10.1021/ja8051427.

Cao, X., Tan, C., Zhang, X., Zhao, W., and Zhang, H. (2016). Solution-processed two-dimensional metal dichalcogenide-based nanomaterials for energy storage and conversion. Adv. Mater. *28*, 6167–6196. https://doi.org/10.1002/adma.201504833.

Chen, Y., Liu, H., Tian, Y., Du, Y., Ma, Y., Zeng, S., Gu, C., Jiang, T., and Zhou, J. (2020). In situ recyclable surface-enhanced Raman scattering-based detection of multicomponent pesticide residues on fruits and vegetables by the flower-like MoS_2@ Ag hybrid substrate. ACS Appl. Mater. Interf. *12*, 14386–14399. https://doi.org/10.1021/acsami.9b22725.

Choudhary, K., Kalish, I., Beams, R., and Tavazza, F. (2017). High-throughput identification and characterization of two-dimensional materials using density functional theory. Sci. Rep. *7*, 1–16. https://doi.org/10.1038/s41598-017-05402-0.

Coleman, J.N. (2009). Liquid-phase exfoliation of nanotubes and graphene. Adv. Funct. Mater. *19*, 3680–3695. https://doi.org/10.1002/adfm.200901640.

Coleman, J.N., Lotya, M., O'Neill, A., Bergin, S.D., King, P.J., Khan, U., Young, K., Gaucher, A., De, S., and Smith, R.J. (2011). Two-dimensional nanosheets produced by liquid exfoliation of layered materials. Science *331*, 568–571. https://doi.org/10.1126/science.1194975.

Dathbun, A., Kim, Y., Kim, S., Yoo, Y., Kang, M.S., Lee, C., and Cho, J.H. (2017). Large-area CVD-grown sub-2V ReS_2 transistors and logic gates. Nano Lett. *17*, 2999–3005. https://doi.org/10.1021/acs.nanolett.7b00315.

DiStefano, J.G., Murthy, A.A., Lescott, C.J., Dos Reis, R., Li, Y., and Dravid, V.P. (2020). Au@MoS_2@WS_2 core–shell architectures: combining vapor phase and solution-based approaches. J. Phys. Chem. C *124*, 2627–2633. https://doi.org/10.1021/acs.jpcc.9b11365.

Goswami, T., Rani, R., Hazra, K.S., and Ghosh, H.N. (2019). Ultrafast carrier dynamics of the exciton and trion in MoS_2 monolayers followed by dissociation dynamics in Au@ MoS_2 2D hetero-interfaces. J. Phys. Chem. Lett. *10*, 3057–3063. https://doi.org/10.1021/acs.jpclett.9b01022.

Grieger, S., Szydłowska, B.M., Rao, V.J., Steinmann, E., Dodds, M., Gholamvand, Z., Duesberg, G.S., Zaumseil, J., and Backes, C. (2020). Site-selective oxidation of monolayered liquid-exfoliated WS_2 by shielding the basal plane through adsorption of a facial amphiphile. Angew. Chem. *132*, 13889–13896. https://doi.org/10.1002/ange.202005730.

Guardia, L., Paredes, J.I., Rozada, R., Villar-Rodil, S., Martínez-Alonso, A., and Tascón, J.M. (2014). Production of aqueous dispersions of inorganic graphene analogues by exfoliation and stabilization with non-ionic surfactants. RSC Adv. *4*, 14115–14127. https://doi.org/10.1039/C4RA00212A.

Guo, J., Li, S., He, Z., Li, Y., Lei, Z., Liu, Y., Huang, W., Gong, T., Ai, Q., and Mao, L. (2019). Near-infrared photodetector based on few-layer MoS_2 with sensitivity enhanced by localized surface plasmon resonance. Appl. Surf. Sci. *483*, 1037–1043. https://doi.org/10.1016/j.apsusc.2019.04.044.

Harvey, A., Backes, C., Gholamvand, Z., Hanlon, D., McAteer, D., Nerl, H.C., McGuire, E., Seral-Ascaso, A., Ramasse, Q.M., and McEvoy, N. (2015). Preparation of gallium sulfide nanosheets by liquid exfoliation and their application as hydrogen evolution catalysts. Chem. Mater. *27*, 3483–3493. https://doi.org/10.1021/acs.chemmater.5b00910.

Hassan, K., Nine, M.J., Tung, T.T., Stanley, N.J., Yap, P.L., Rastin, H., Yu, L., and Losic, D. (2020). Functional inks and extrusion-based 3D printing of 2D materials: a review of current research and applications. Nanoscale *12*, 19007–19042. https://doi.org/10.1039/D0NR04933F.

Huh, W., Lee, D., and Lee, C.H. (2020). Memristors based on 2D materials as an artificial synapse for neuromorphic electronics. Adv. Mater. *32*, 2002092. https://doi.org/10.1002/adma.202002092.

Jariwala, D., Sangwan, V.K., Lauhon, L.J., Marks, T.J., and Hersam, M.C. (2014). Emerging device applications for semiconducting two-dimensional transition metal dichalcogenides.

ACS Nano *8*, 1102–1120. https://doi.org/10.1021/nn500064s.

Kang, J., Seo, J.-W.T., Alducin, D., Ponce, A., Yacaman, M.J., and Hersam, M.C. (2014). Thickness sorting of two-dimensional transition metal dichalcogenides via copolymer-assisted density gradient ultracentrifugation. Nat. Commun. *5*, 5478. https://doi.org/10.1038/ncomms6478.

Kaur, J., Singh, M., Dell'Aversana, C., Benedetti, R., Giardina, P., Rossi, M., Valadan, M., Vergara, A., Cutarelli, A., and Montone, A.M.I. (2018). Biological interactions of biocompatible and water-dispersed MoS_2 nanosheets with bacteria and human cells. Sci. Rep. *8*, 1–15. https://doi.org/10.1038/s41598-018-34679-y.

Kelly, A.G., O'Suilleabhain, D., Gabbett, C., and Coleman, J.N. (2021). The electrical conductivity of solution-processed nanosheet networks. Nat. Rev. Mater. 1–18. https://doi.org/10.1038/s41578-021-00386-w.

Kim, J., Byun, S., Smith, A.J., Yu, J., and Huang, J. (2013). Enhanced electrocatalytic properties of transition-metal dichalcogenides sheets by spontaneous gold nanoparticle decoration. J. Phys. Chem. Lett. *4*, 1227–1232. https://doi.org/10.1021/jz400507t.

Kim, J., Kim, S., Cho, Y.S., Choi, M., Jung, S.-H., Cho, J.H., Whang, D., and Kang, J. (2021). Solution-processed MoS_2 film with functional interfaces via precursor-assisted chemical welding. ACS Appl. Mater. Interf. *13*, 12221–12229. https://doi.org/10.1021/acsami.1c00159.

Lee, Y., Kim, H., Lee, J., Yu, S.H., Hwang, E., Lee, C., Ahn, J.-H., and Cho, J.H. (2016). Enhanced Raman scattering of rhodamine 6G films on two-dimensional transition metal dichalcogenides correlated to photoinduced charge transfer. Chem. Mater. *28*, 180–187. https://doi.org/10.1021/acs.chemmater.5b03714.

Li, J., Han, J., Li, H., Fan, X., and Huang, K. (2020a). Large-area, flexible broadband photodetector based on WS_2 nanosheets films. Mater. Sci. Semicond. Process. *107*, 104804. https://doi.org/10.1016/j.mssp.2019.104804.

Li, J., Nie, C., Sun, F., Tang, L., Zhang, Z., Zhang, J., Zhao, Y., Shen, J., Feng, S., and Shi, H. (2020b). Enhancement of the photoresponse of monolayer MoS_2 photodetectors induced by a nanoparticle grating. ACS Appl. Mater. Interf. *12*, 8429–8436. https://doi.org/10.1021/acsami.9b20506.

Lin, J., Li, H., Zhang, H., and Chen, W. (2013). Plasmonic enhancement of photocurrent in MoS_2 field-effect-transistor. Appl. Phys. Lett. *102*, 203109. https://doi.org/10.1063/1.4807658.

Lin, Z., Luo, P., Zeng, W., Lai, H., Xie, W., Deng, W., and Luo, Z. (2020). Improvement of photoelectric properties of MoS_2/WS_2 heterostructure photodetector with interlayer of Au nanoparticles. Opt. Mater. *108*, 110191. https://doi.org/10.1016/j.optmat.2020.110191.

LináLi, B., LináZou, H., QunáLuo, H., TaiáLeong, D., and BingáLi, N. (2020). Layered MoS_2 defect-driven in situ synthesis of plasmonic gold nanocrystals visualizes the planar size and interfacial diversity. Nanoscale *12*, 11979–11985. https://doi.org/10.1039/D0NR02838J.

Liu, B., Zhao, C., Chen, X., Zhang, L., Li, Y., Yan, H., and Zhang, Y. (2019). Self-powered and fast photodetector based on graphene/$MoSe_2$/Au heterojunction. Superlattice. Microst. *130*, 87–92. https://doi.org/10.1016/j.spmi.2019.04.021.

Lobo, K., Sahoo, P., Kurapati, R., Krishna, K.,V., Patil, V., Pandit, A., and Matte, H.R. (2021). Additive-free aqueous dispersions of two-dimensional materials with glial cell compatibility and enzymatic degradability. Chem. Eur. J. *27*, 7434–7443. https://doi.org/10.1002/chem.202005491.

Lobo, K., Trivedi, S., and Matte, H.R. (2019). Highly concentrated and stabilizer-free transition-metal dichalcogenide dispersions in low-boiling point solvent for flexible electronics. Nanoscale *11*, 10746–10755.

Lombardi, J.R., and Birke, R.L. (2012). The theory of surface-enhanced Raman scattering. J. Chem. Phys. *136*, 144704. https://doi.org/10.1021/jp5020675.

Lombardi, J.R., and Birke, R.L. (2014). Theory of surface-enhanced Raman scattering in semiconductors. J. Phys. Chem. C *118*, 11120–11130. https://doi.org/10.1021/jp5020675.

Lotya, M., Hernandez, Y., King, P.J., Smith, R.J., Nicolosi, V., Karlsson, L.S., Blighe, F.M., De, S., Wang, Z., and McGovern, I. (2009). Liquid phase production of graphene by exfoliation of graphite in surfactant/water solutions. J. Am. Chem. Soc. *131*, 3611–3620. https://doi.org/10.1021/ja807449u.

Lu, J., Lu, J.H., Liu, H., Liu, B., Gong, L., Tok, E.S., Loh, K.P., and Sow, C.H. (2015). Microlandscaping of Au nanoparticles on few-layer MoS_2 films for chemical sensing. Small *11*, 1792–1800. https://doi.org/10.1002/smll.201402591.

Lu, P., Lang, J., Weng, Z., Rahimi-Iman, A., and Wu, H. (2018). Hybrid structure of 2D layered GaTe with Au nanoparticles for ultrasensitive detection of aromatic molecules. ACS Appl. Mater. Interf. *10*, 1356–1362. https://doi.org/10.1021/acsami.7b14121.

Lu, X., Stepanov, P., Yang, W., Xie, M., Aamir, M.A., Das, I., Urgell, C., Watanabe, K., Taniguchi, T., and Zhang, G. (2019). Superconductors, orbital magnets and correlated states in magic-angle bilayer graphene. Nature *574*, 653–657. https://doi.org/10.1038/s41586-019-1695-0.

Lv, K., Si, H., Liu, J., Zhu, T., Xia, Y., Chen, S., Zhao, Y., and Yang, C. (2020). Plasmonic filters based on MoS_2@Au/Ag hybrids: controllable separation, preconcentration, and sensitive SERS detection. J. Alloys Compd. *846*, 156438. https://doi.org/10.1016/j.jallcom.2020.156438.

Ma, B., Martín, C., Kurapati, R., and Bianco, A. (2020). Degradation-by-design: how chemical functionalization enhances the biodegradability and safety of 2D materials. Chem. Soc. Rev. *49*, 6224–6247. https://doi.org/10.1039/C9CS00822E.

Ma, R., and Sasaki, T. (2015). Two-dimensional oxide and hydroxide nanosheets: controllable high-quality exfoliation, molecular assembly, and exploration of functionality. Acc. Chem. Res. *48*, 136–143. https://doi.org/10.1021/ar500311w.

Maleski, K., Mochalin, V.N., and Gogotsi, Y. (2017). Dispersions of two-dimensional titanium carbide MXene in organic solvents. Chem. Mater. *29*, 1632–1640. https://doi.org/10.1021/acs.chemmater.6b04830.

McManus, D., Dal Santo, A., Selvasundaram, P., Krupke, R., LiBassi, A., and Casiraghi, C. (2018). Photocurrent study of all-printed photodetectors on paper made of different transition metal dichalcogenide nanosheets. Flex. Print. Electron. *3*, 034005. https://doi.org/10.1088/2058-8585/aaddb5.

McManus, D., Vranic, S., Withers, F., Sanchez-Romaguera, V., Macucci, M., Yang, H., Sorrentino, R., Parvez, K., Son, S.-K., Iannaccone, G., et al. (2017). Water-based and biocompatible 2D crystal inks for all-inkjet-printed heterostructures. Nat. Nanotechnol. *12*, 343–350. https://doi.org/10.1038/nnano.2016.281.

Miao, J., Hu, W., Jing, Y., Luo, W., Liao, L., Pan, A., Wu, S., Cheng, J., Chen, X., and Lu, W. (2015). Surface plasmon-enhanced photodetection in few layer MoS_2 phototransistors with Au nanostructure arrays. Small *11*, 2392–2398. https://doi.org/10.1002/smll.201403422.

Nicolai, S.H., and Rubim, J.C. (2003). Surface-enhanced resonance Raman (SERR) spectra of methylene blue adsorbed on a silver electrode. Langmuir *19*, 4291–4294. https://doi.org/10.1021/la034076v.

Nicolosi, V., Chhowalla, M., Kanatzidis, M.G., Strano, M.S., and Coleman, J.N. (2013). Liquid exfoliation of layered materials. Science *340*, 1226419. https://doi.org/10.1126/science.1226419.

O'Neill, A., Khan, U., and Coleman, J.N. (2012). Preparation of high concentration dispersions of exfoliated MoS_2 with increased flake size. Chem. Mater. *24*, 2414–2421. https://doi.org/10.1021/cm301515z.

Ogilvie, S.P., Large, M.J., O'Mara, M.A., Lynch, P.J., Lee, C.L., King, A.A., Backes, C., and Dalton, A.B. (2019). Size selection of liquid-exfoliated 2D nanosheets. 2D Mater. *6*, 031002. https://doi.org/10.1088/2053-1583/ab0dc3.

Polyakov, A.Y., Yadgarov, L., Popovitz-Biro, R., Lebedev, V.A., Pinkas, I., Rosentsveig, R., Feldman, Y., Goldt, A.E., Goodilin, E.A., and Tenne, R. (2014). Decoration of WS_2 nanotubes and fullerene-like MoS2 with gold nanoparticles. J. Phys. Chem. C *118*, 2161–2169. https://doi.org/10.1021/jp407388h.

Pramanik, A., Gao, Y., Gates, K., Begum, S., and Ray, P.C. (2019). Giant chemical and excellent synergistic Raman enhancement from a 3D $MoS_{2-x}O_x$–Gold nanoparticle hybrid. ACS Omega *4*, 11112–11118. https://doi.org/10.1021/acsomega.9b00866.

Pulikodan, V.K., Alexander, A., Pillai, A.B., and Namboothiry, M.A. (2020). Photoresponse of solution-processed molybdenum disulfide nanosheet-based photodetectors. ACS Appl. Nano Mater. *3*, 10057–10066. https://doi.org/10.1021/acsanm.0c02058.

Rahmati, B., Hajzadeh, I., Taheri, M., Karimzadeh, R., Mohajerzadeh, S., and Mohseni, S. (2019). Plasmonic improvement photoresponse of vertical-MoS_2 nanostructure photodetector by Au

nanoparticles. Appl. Surf. Sci. *490*, 165–171. https://doi.org/10.1016/j.apsusc.2019.06.058.

Secor, E.B., Ahn, B.Y., Gao, T.Z., Lewis, J.A., and Hersam, M.C. (2015). Rapid and versatile photonic annealing of graphene inks for flexible printed electronics. Adv. Mater. *27*, 6683–6688. https://doi.org/10.1002/adma.201502866.

Secor, E.B., Prabhumirashi, P.L., Puntambekar, K., Geier, M.L., and Hersam, M.C. (2013). Inkjet printing of high conductivity, flexible graphene patterns. J. Phys. Chem. Lett. *4*, 1347–1351. https://doi.org/10.1021/jz400644c.

Selamneni, V., Raghavan, H., Hazra, A., and Sahatiya, P. (2021). MoS_2/Paper decorated with metal nanoparticles (Au, Pt, and Pd) based plasmonic-enhanced broadband (Visible-NIR) flexible photodetectors. Adv. Mater. Interf. *8*, 2001988. https://doi.org/10.1002/admi.202001988.

Seo, B., Jung, G.Y., Sa, Y.J., Jeong, H.Y., Cheon, J.Y., Lee, J.H., Kim, H.Y., Kim, J.C., Shin, H.S., and Kwak, S.K. (2015). Monolayer-precision synthesis of molybdenum sulfide nanoparticles and their nanoscale size effects in the hydrogen evolution reaction. ACS Nano *9*, 3728–3739. https://doi.org/10.1021/acsnano.5b00786.

Seo, J.-W.T., Zhu, J., Sangwan, V.K., Secor, E.B., Wallace, S.G., and Hersam, M.C. (2019). Fully inkjet-printed, mechanically flexible MoS_2 nanosheet photodetectors. ACS Appl. Mater. Interf. *11*, 5675–5681. https://doi.org/10.1021/acsami.8b19817.

Singha, S.S., Mondal, S., Bhattacharya, T.S., Das, L., Sen, K., Satpati, B., Das, K., and Singha, A. (2018). Au nanoparticles functionalized 3D-MoS_2 nanoflower: an efficient SERS matrix for biomolecule sensing. Biosens. Bioelectron. *119*, 10–17. https://doi.org/10.1016/j.bios.2018.07.061.

Song, B., He, K., Yuan, Y., Sharifi-Asl, S., Cheng, M., Lu, J., Saidi, W.A., and Shahbazian-Yassar, R. (2018). In situ study of nucleation and growth dynamics of Au nanoparticles on MoS_2 nanoflakes. Nanoscale *10*, 15809–15818. https://doi.org/10.1039/C8NR03519A.

Sreeprasad, T., Nguyen, P., Kim, N., and Berry, V. (2013). Controlled, defect-guided, metal-nanoparticle incorporation onto MoS_2 via chemical and microwave routes: electrical, thermal, and structural properties. Nano Lett. *13*, 4434–4441. https://doi.org/10.1021/nl402278y.

Su, S., Zhang, C., Yuwen, L., Chao, J., Zuo, X., Liu, X., Song, C., Fan, C., and Wang, L. (2014). Creating SERS hot spots on MoS_2 nanosheets with in situ grown gold nanoparticles. ACS Appl. Mater. Interf. *6*, 18735–18741. https://doi.org/10.1021/am5043092.

Sun, K., Gu, Z., Katsura, H., and Sarma, S.D. (2011). Nearly flatbands with nontrivial topology. Phys. Rev. Lett. *106*, 236803. https://doi.org/10.1103/PhysRevLett.106.236803.

Sun, L., Hu, H., Zhan, D., Yan, J., Liu, L., Teguh, J.S., Yeow, E.K., Lee, P.S., and Shen, Z. (2014). Plasma modified MoS_2 nanoflakes for surface enhanced Raman scattering. Small *10*, 1090–1095. https://doi.org/10.1002/smll.201300798.

Tao, L., Li, Z., Chen, K., Zhou, Y., Li, H., Wang, X., Zhan, R., Hou, X., Zhao, Y., and Xu, J. (2021). A spontaneously formed plasmonic-$MoTe_2$ hybrid platform for ultrasensitive Raman enhancement. Cell Rep. Phys. Sci. *2*, 100526. https://doi.org/10.1016/j.xcrp.2021.100526.

Tegegne, W.A., Su, W.-N., Tsai, M.-C., Beyene, A.B., and Hwang, B.-J. (2020). Ag nanocubes decorated 1T-MoS_2 nanosheets SERS substrate for reliable and ultrasensitive detection of pesticides. Appl. Mater. Today *21*, 100871. https://doi.org/10.1016/j.apmt.2020.100871.

Teweldebrhan, D., Goyal, V., and Balandin, A.A. (2010). Exfoliation and characterization of bismuth telluride atomic quintuples and quasi-two-dimensional crystals. Nano Lett. *10*, 1209–1218. https://doi.org/10.1021/nl903590b.

Tsai, M.-L., Su, S.-H., Chang, J.-K., Tsai, D.-S., Chen, C.-H., Wu, C.-I., Li, L.-J., Chen, L.-J., and He, J.-H. (2014). Monolayer MoS_2 heterojunction solar cells. ACS Nano *8*, 8317–8322. https://doi.org/10.1021/nn502776h.

Tu, C.-Y., and Wu, J.M. (2021). Localized surface plasmon resonance coupling with piezophototronic effect for enhancing hydrogen evolution reaction with Au@MoS_2 nanoflowers. Nano Energy *87*, 106131. https://doi.org/10.1016/j.nanoen.2021.106131.

Varrla, E., Backes, C., Paton, K.R., Harvey, A., Gholamvand, Z., McCauley, J., and Coleman, J.N. (2015). Large-scale production of size-controlled MoS_2 nanosheets by shear exfoliation. Chem. Mater. *27*, 1129–1139. https://doi.org/10.1021/cm5044864.

Wang, H., Yu, L., Lee, Y.-H., Shi, Y., Hsu, A., Chin, M.L., Li, L.-J., Dubey, M., Kong, J., and Palacios, T. (2012a). Integrated circuits based on bilayer MoS_2 transistors. Nano Lett. *12*, 4674–4680. https://doi.org/10.1021/nl302015v.

Wang, M., Xu, X., Ge, Y., Dong, P., Baines, R., Ajayan, P.M., Ye, M., and Shen, J. (2017). Surface tension components ratio: an efficient parameter for direct liquid phase exfoliation. ACS Appl. Mater. Interf. *9*, 9168–9175. https://doi.org/10.1021/acsami.6b16578.

Wang, Q.H., Kalantar-Zadeh, K., Kis, A., Coleman, J.N., and Strano, M.S. (2012b). Electronics and optoelectronics of two-dimensional transition metal dichalcogenides. Nat. Nanotechnol. *7*, 699–712. https://doi.org/10.1038/nnano.2012.193.

Wang, T., Gao, D., Zhuo, J., Zhu, Z., Papakonstantinou, P., Li, Y., and Li, M. (2013). Size-dependent enhancement of electrocatalytic oxygen-reduction and hydrogen-evolution performance of MoS_2 particles. Chem. Eur. J. *19*, 11939–11948. https://doi.org/10.1002/chem.201301406.

Xiao, G.-N., and Man, S.-Q. (2007). Surface-enhanced Raman scattering of methylene blue adsorbed on cap-shaped silver nanoparticles. Chem. Phys. Lett. *447*, 305–309. https://doi.org/10.1016/j.cplett.2007.09.045.

Yin, Z., Chen, B., Bosman, M., Cao, X., Chen, J., Zheng, B., and Zhang, H. (2014). Au nanoparticle-modified MoS2 nanosheet-based photoelectrochemical cells for water splitting. Small *10*, 3537–3543. https://doi.org/10.1002/smll.201400124.

Yuan, Y., Yang, B., Jia, F., and Song, S. (2019). Reduction mechanism of Au metal ions into Au nanoparticles on molybdenum disulfide. Nanoscale *11*, 9488–9497. https://doi.org/10.1039/C8NR09420A.

Zhou, K.G., Mao, N.N., Wang, H.X., Peng, Y., and Zhang, H.L. (2011). A mixed-solvent strategy for efficient exfoliation of inorganic graphene analogues. Angew. Chem. Intern. Ed. *123*, 11031–11034. https://doi.org/10.1002/anie.201105364.

STAR★METHODS

KEY RESOURCES TABLE

REAGENT or RESOURCE	SOURCE	IDENTIFIER
Chemicals, peptides, and recombinant proteins		
Molybdenum disulfide	Alfa Aesar	CAS No. 1317-33-5
Molybdenum diselenide	Alfa Aesar	CAS No. 12058-18-3
Tungsten disulfide	Sigma Aldrich	CAS No. 12138-09-9
Tungsten diselenide	Alfa Aesar	CAS No. 12067-46-8
2-Butanone	Finar	CAS No. 78-93-3
Chloroauric acid	Sigma Aldrich	CAS No. 27988-77-8
Software and algorithms		
Origin	www.originlab.com	Origin 2018
Adobe Illustrator	https://www.adobe.com/in/products/illustrator.html	Adobe Illustrator CC 2015
ImageJ	https://imagej.nih.gov/ij/download.html	ImageJ 1.51j8
Origin	www.originlab.com	Origin 2018
Other		
Bath sonicator	Elma	https://www.elma-ultrasonic.com/produkte/ultraschallgeraete/elmasonic-ti-h#tabs|p21:features
X-ray diffractometer	Rigaku	https://www.rigaku.com/products/xrd/smartlab
Field emission scanning electron microscope	Tescan	https://www.tescan.com/product/sem-for-materials-science-tescan-mira/
UV-Visible spectrophotometer	Perkin-Elmer	https://www.perkinelmer.com/
Particle size analyser	Malvern Panalytical	https://www.malvernpanalytical.com/en/support/product-support/zetasizer-range/zetasizer-nano-range/zetasizer-nano-zs
Raman spectrometer	Horiba	https://www.horiba.com/int/products/detail/action/show/Product/xploratm-plus-1528/
Transmission electron microscope	Thermo-Scientific	https://www.fei.com/products/tem/talos/#gsc.tab=0
Electrical characterization system	Keithley	https://www.tek.com/en/keithley-4200a-scs-parameter-analyzer
Probe station	FormFactor	https://www.formfactor.com/product/probe-systems/150-mm-systems/mps150/

RESOURCE AVAILABILITY

Materials availability

This study did not generate any new unique reagents.

Date and code availability

The data reported in this paper can be shared by the lead contact upon request.

METHOD DETAILS

Exfoliation and size-selection

Bulk MoS_2 powders (Alfa Aesar, 325 mesh, 99%) were sonicated in 2-butanone (Finar, 99%) at a concentration of 30 mg mL^{-1} using an Elmasonic TI-H5 bath sonicator at 45 kHz for 30 h under cold water circulation. This dispersion is then subjected to cascaded centrifugation at successively increasing speeds between 1000 and 5000 rpm on a REMI PR-24 centrifuge to obtain sediments of size-selected nanosheets. These

sediments in the form of a paste are then dried in to powder in a hot air oven at 80°C, and then re-dispersed at desired concentrations in deionized water by mild sonication to obtain aqueous size-selected nanosheet dispersions. Aqueous dispersions of $MoSe_2$, WS_2 and WSe_2 were prepared in a similar manner for sediments obtained between 1000 and 5000 rpm, without size-selection. These protocols have been demonstrated with extensive characterization in these following articles (Lobo et al., 2019, 2021).

Au nanoparticle decoration

Employing the spontaneous reduction mechanism of $HAuCl_4$ by MoS_2 nanosheets, Au nanoparticle decoration was carried out by reacting 1 mL of size-selected MoS_2 dispersion of 0.2 mg mL^{-1} concentration with 1 mL of $HAuCl_4$ solution of 2 (2.5 mM) and 4 (5 mM) equivalents. The reaction was allowed to proceed for 18 h, after which unreacted $HAuCl_4$ was removed by iteratively centrifuging for 10 min at 5000 rpm and washing with deionized water for 3 times. The washed sediments containing the decorated nanosheets were then re-dispersed in 2 mL of deionized water. Au decoration of aqueously dispersed $MoSe_2$, WS_2 and WSe_2 nanosheets were carried out by reacting the dilute dispersions with $HAuCl_4$ solution.

Characterization techniques

Substrates for X-ray diffraction were prepared by drop-casting the samples onto cleaned glass slides and drying at 80°C. Diffraction patterns were obtained on a Rigaku SmartLab with a Cu source, at a scan rate of 1° min^{-1} with step size of 0.01°. UV-Visible spectra of dispersions were recorded using a Perkin Elmer Lambda 750 spectrometer. Field emission scanning electron microscopy was carried out on a Tescan Mira3 by drop casting the samples onto Si substrates at 80°C. Dynamic light scattering and determination of zeta potentials were carried out on a Malvern Zetasizer NanoZS. Transmission electron microscopy was carried out on a Thermo Scientific Talos (200 kV) by coating lacey carbon grids with dilute dispersions.

Surface enhanced raman scattering

Substrates for surface enhanced Raman scattering were prepared by drop-casting 50 μL of the dispersions onto glass slides held at 80°C on a hotplate. Once dried, 40 μL of methylene blue (10 μM) was added. A Horiba XploRa Plus Raman spectrometer was used for acquiring the spectra, using 2 accumulations for an acquisition time of 4 s at a laser power of 0.3 mW with a grating of 1200 grooves mm^{-1}. The hole and slit width were maintained at 300 and 100 μm respectively.

Determination of enhancement factor (EF)

The formula to determine the EF of SERS substrates is given by

$$EF = (I_{SERS}/I_{Raman}) \times (N_{Raman}/N_{SERS})$$

Under the experimental conditions used, I_{Raman}, N_{Raman} and N_{SERS} are unchanged, providing a factor for multiplication of the observed I_{SERS} in the case of each sample in order to determine the EF.

I_{Raman} (Signal intensity for dye powder) is straightforward to obtain, and was found to be 340 counts. To determine the number of molecules excited in the bulk powder, the diameter of the laser spot and penetration depth need to be calculated.

$$\text{Diameter of focused laser spot} = 1.22 * (\lambda/NA)$$

For 638 nm laser and 0.5 NA of the lens used in the experiments, the diameter is computed to be 1.55 μm. The radius would then be r = 0.778 μm.

$$\text{The penetration depth is calculated by } d = 2\,\lambda/(NA)^2$$

This depth is calculated to be 5.10 μm.

The volume (assumed to be a cylinder) excited by the laser can therefore be calculated as

$$V = \pi r^2 d$$

$$V = \pi(0.778\ \mu m)^2\ (5.10\ \mu m)$$

$$= 9.709\ \mu m^3$$

To obtain the number of molecules excited in this volume,

$$N_{Raman} = V * \rho_{MB} * N_A/M_{MB}$$

Where ρ_{MB} is the density of methylene blue (1757 kg m^{-3}), N_A is the Avogadro number and M_{MB} is the molecular weight of methylene blue (319.9 g mol^{-1}).

Substituting these values,

$$N_{Raman} = 9.709\ \mu m^3 * 1.757\ g\ mL^{-1} * 6.022 * 10^{22}\ mol^{-1}/319.9\ g\ mol^{-1}$$

$$= 3.213 * 10^{10}$$

In order to compute the number of molecules excited in SERS, monolayer coverage of dye molecules was assumed.

$$\text{The area of one methylene blue molecule} = 0.8723\ nm^2$$

$$\text{The area under the laser spot is} = \pi r^2 = 1.9 * 10^{-12}\ m^2$$

Therefore, the number of molecules under illumination (assuming monolayer coverage on the substrate) is found to be

$$= 1.9 * 10^{-12}\ m^2/0.8723\ nm^2$$

$$= 2.18 * 10^6$$

By substituting these computed values, a factor of 43.4 was obtained for multiplication with the observed I_{SERS} to calculate the value of EF.

Solution-processed photodetectors

Photodetectors were fabricated by spray coating 5 mL of dispersions (0.2 mg mL^{-1}) of the undecorated MoS_2 nanosheets onto glass slides with Au gap electrodes. The substrates were held at 80°C on a hotplate at a distance of 10 cm, and spraying was carried out at a pressure of 10psi. The spray coated devices were then decorated with Au nanoparticles by dipping the substrates in to a solution of 1 mM $HAuCl_4$ for a defined period of time. After dipping, the substrates were immediately washed with running deionized water and dried on a hotplate held at 80°C and later stored under dessication. The electrical characterization of the devices were carried out on a Keithley 4200SCS paired with a Cascade Microtech EPS-150 probe station. A 532 nm laser was used as the light source.